Crystal field and hyperfine structure of ^{167}Er^{3+} in YPO$_4$:Er single crystals: High-resolution optical and EPR spectroscopy

M. N. Popova,[1] S. A. Klimin,[1,*] S. A. Moiseev,[2] K. I. Gerasimov,[2] M. M. Minnegaliev,[2] E. I. Baibekov,[2,3]
G. S. Shakurov,[4] M. Bettinelli,[5] and M. C. Chou[6]

[1]*Institute of Spectroscopy, Russian Academy of Sciences, 5, Fizicheskaya Str., Troitsk, Moscow 108840, Russian Federation*

[2]*Kazan Quantum Center, Kazan National Research Technical University named after A.N. Tupolev-KAI, 10 K. Marx Str., Kazan 420111, Russia*

[3]*Kazan (Volga Region) Federal University, 18 Kremlyovskaya Str., Kazan 420008, Russia*

[4]*Zavoisky Physical Technical Institute, FRC Kazan Scientic Center of the Russian Academy of Sciences, ul. Sibirskii trakt 10/7, Kazan, 420029, Russia*

[5]*Dipartimento di Biotecnologie, University of Verona and INSTM, Strada Le Grazie 15, Verona 37134, Italy*

[6]*Department of Materials and Optoelectronic Science, Center of Crystal Research, National Sun Yat-Sen University, 70, Lien-Hai Rd., Kaohsiung 80424, Taiwan*

We report on a high-resolution optical and magneto-optical spectroscopy, luminescence, and electron paramagnetic resonance (EPR) studies of yttrium orthophosphate single crystals doped with erbium, which are promising telecom-wavelength materials for applications in quantum electronics and quantum information processing. An observation of the hyperfine structure in optical spectra of ^{167}Er isotope in Er : YPO$_4$ is presented. Energies and symmetries of 40 crystal-field levels of Er^{3+} in Er : YPO$_4$ and g factors of some of them were determined and successfully modeled on the basis of crystal-field calculations. The obtained set of crystal-field parameters was used in modeling the hyperfine structure observed in the optical and EPR spectra of Er : YPO$_4$ single crystals.

I. INTRODUCTION

The orthovanadates AVO$_4$(A = Y, Gd, Lu) and orthophosphates APO$_4$(A = Y, Lu) with zircon structure, pure or doped with rare-earth (RE) ions, exhibit unique physicochemical and optical properties, which makes them interesting for numerous applications such as laser [1–6] and Raman-laser [7] hosts, scintillators for γ- and x-ray detection [8,9], thermophosphors for remote temperature measurements [10], up- and down-conversion (quantum cutting) materials for fluorescent lamps, plasma display panels, solar cells, security markers [11–14], biolabels, drug carriers, and agents in photodynamic therapy [15], etc. All the vanadate crystals can be grown by the Czochralski method and large single crystals of good optical quality are available [1]. The most well-developed vanadate Nd : YVO$_4$ crystal is among the best commercial materials for diode-pumped continuous-wave, Q-switched, and mode-locked lasers but Nd^{3+}- and Yb^{3+}-doped GdVO$_4$, LuVO$_4$, and mixed Gd$_x$Y$_{1-x}$VO$_4$ and Lu$_x$Gd$_{1-x}$VO$_4$ crystals are intensively studied for different laser applications, including in the high-power laser field [1]. Tm^{3+}-doped GdVO$_4$ and LuVO$_4$ crystals also demonstrate an efficient laser performance [2,3]. Orthophosphates melt incongruently and cannot be grown by the conventional Czochralski method, and it is extremely difficult to produce high-quality single

crystals of large sizes. Recently, a Chinese group from Qingdao succeeded in growing good-quality single crystals of Yb-doped LuPO$_4$ [4,5] and YPO$_4$ [6] single crystals using the high-temperature solution-melt method. Continuous-wave [4] and Q-switched [5] high-power efficient laser operation of a miniature Yb : LuPO$_4$ crystal rod was reported. Efficient continuous-wave laser action was achieved under diode end-pumping conditions of a plate-shaped Yb : YPO$_4$ 1.0-mm thick crystal [6].

This success draws attention to the Er : YPO$_4$ crystal, which could be a good candidate for lasing at the telecom wavelength 1.5 μm. Using Er : YPO$_4$ in quantum memory devices to increase the range of cryptographic communication lines [16–18] could be another attractive application. It is important to note that an optical quantum memory has already been successfully realized using hyperfine levels of Nd^{3+} in Nd : YVO$_4$ crystals [19,20]. Unlike vanadium, the most common (99.7%) isotope of which ^{51}V has a large nuclear spin $I = 7/2$, phosphorus is a monoisotopic element with nuclear spin $I = 1/2$ (as in yttrium). Due to this circumstance, YPO$_4$ could turn out to be a better matrix for quantum memory than YVO$_4$. In addition, the resolved hyperfine structure (HFS) was observed in the absorption spectra of Ho : YPO$_4$ crystals [21]. The resolved HFS is also favorable for the implementation of the off-resonant Raman-echo [22] and gradient-echo [23] protocols of optical quantum memory.

For applications in quantum memory devices, the knowledge of HFS of the crystal-field (CF) levels is essential. We

---

*Corresponding author: klimin@isan.troitsk.ru

are not aware of any experimental information on the HFS in the spectra of Er : YPO_4. The only stable odd isotope ^{167}Er has the nuclear spin $I = 7/2$ and the natural abundance of 22.87%. Other five stable isotopes, the most abundant of them being ^{166}Er (33.503%), are even ones with $I = 0$ and, hence, have no HFS of electronic levels. The HFS can be calculated with the help of wave functions of CF levels obtained from CF calculations. However, CF parameters available in literature are contradictory [24–27]. We decided to perform high-resolution optical absorption and luminescence spectroscopy measurements of Er : YPO_4 single crystals, with the aims (i) to look for the HFS in the spectra and (ii) to determine reliable CF parameters for modeling the HFS.

The paper is organized in the following way. In Sec. II we describe the crystal growth and provide information on the equipment and procedures used to measure the EPR and optical spectra. Experimental data on energies, symmetries, g factors, and hyperfine structure of the crystal-field levels of Er^{3+} in Er : YPO_4 obtained from the analysis of high-resolution transmission, luminescence, and EPR spectra are presented in Sec. III. Section IV reports on the crystal-field calculations and the spectra modeling on this basis. Section V briefly summarizes the results.

II. EXPERIMENTAL DETAILS

Yttrium orthophosphate single crystals YPO_4 doped with Er^{3+} ions with concentrations 0.005, 0.01, 0.1, 0.2, 0.4, and 0.7 at.% were grown by the flux method using $Pb_2P_2O_7$ as a high-temperature flux [28]. The procedure involves the dissolution of the rare-earth oxides Er_2O_3 and Y_2O_3 in molten $Pb_2P_2O_7$ at high temperature with spontaneous nucleation and crystal growth of YPO_4 achieved by slow cooling of the solution. High purity Y_2O_3 and Er_2O_3, $(NH_4)_2HPO_4$ and PbO were employed as starting materials. The melt was heated in the platinum crucible to a maximum temperature of $1300\,°C$ and then cooled to $950\,°C$ with a rate of $2\,°C/h$. In all cases, the flux was dissolved using hot diluted HNO_3. Single crystals of good optical quality elongated in the direction of the c axis of the tetragonal structure were obtained. The oriented plates cut from the single crystals with the fixed direction of the c axis had thicknesses from 0.025 to 0.07 cm.

The grown crystals were characterized by the EPR method. The measurements were accomplished with a Bruker EMX plus spectrometer in the X band at 5 K and a homemade broadband EPR spectrometer [29] in the frequency range 36–76 GHz at 4.2 K. In the latter case, generators Γ4-141 and Γ4-142 were used as microwave radiation sources. In the X band, in addition to erbium, Fe^{3+} ions were recorded (at low power level of the microwave generator), as well as weak signals from Gd^{3+} (at a high amplification).

Polarized high-resolution (up to $0.005\,cm^{-1}$) transmission spectra were measured in broad spectral ($5\,000$–$21\,000\,cm^{-1}$) and temperature (4–300 K) ranges using a Fourier spectrometer Bruker IFS 125HR and a closed-cycle cryostat Cryomech ST 403. The temperature was stabilized within $\pm 0.2\,K$. The absolute precision of the wave-number scale was 0.002–$0.02\,cm^{-1}$, depending on the spectral resolution used. The spectra were registered for linearly π-polarized ($\mathbf{E} \perp c \perp \mathbf{k}$) or σ-polarized ($\mathbf{E}\|c\perp\mathbf{k}$) incident radiation ($\mathbf{E}$ and
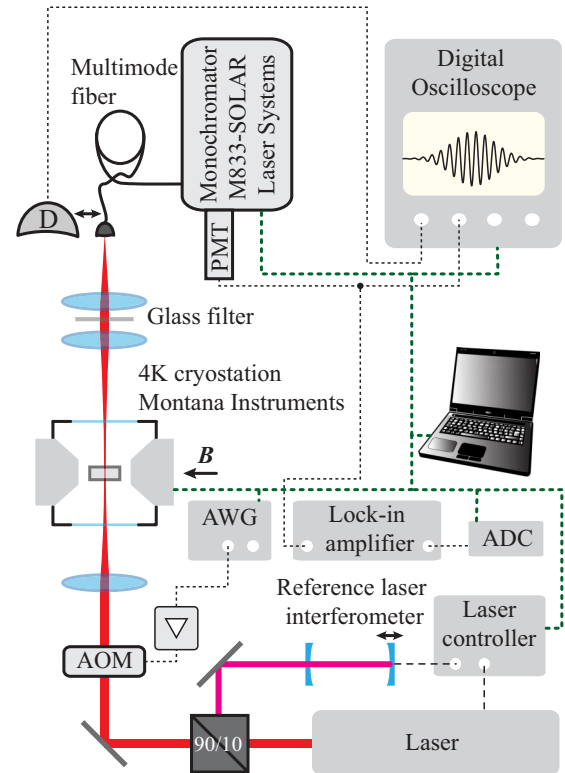

FIG. 1. Experimental setup for recording the absorption and luminescence spectra and kinetics of the luminescence (including in a magnetic field $\mathbf{B}$). AOM – acousto-optic modulator, ADC – analog-to-digital converter, AWG – arbitrary-waveform generator, PMT – photomultiplier, D – detector (avalanche photodiode Thorlabs APD110C/M), Laser – dye TekhnoScan DYE-SF-077 or Ti:Sapphire (TIS-SF-777) or diode (CTL 1500 - TOPTICA Photonics AG) lasers. Green dashed lines denote USB2.0 connections and black dashed lines are for electrical 50-Ω connections between devices.

$\mathbf{k}$ denote the electric field and the wave vector of the incident radiation, respectively, c is the C_4 axis of the crystal).

The spectra and kinetics of the luminescence excited by a dye laser TekhnoScan DYE-SF-077 tuned to the $^4I_{15/2}(\Gamma_7^1) \to {}^4F_{9/2}(\Gamma_6^1)$ ($15279.49\,cm^{-1}$) transition of Er^{3+} were registered. A simplified scheme of the experimental setup is shown in Fig. 1. The intensity of the laser beam was modulated and the pulses were prepared using an acousto-optical modulator (AOM). The samples were cooled in a Montana Instruments helium-free optical cryostat system. The luminescence decay was detected with a Thorlabs avalanche photodiode APD110C/M. Spectra of luminescence were measured using M833 Solar Laser Systems monochromator and a thermoelectrically cooled photomultiplier (PMT) Hamamatsu H12397-75.

In the high-resolution magneto-optical absorption studies, the samples of Er : YPO_4 were cooled and subjected to magnetic fields $\mathbf{B}\|c$ and $\mathbf{B}\perp c$, the values of which could be set between -0.7 and 0.7 T using an add-on magneto-optical module of the Montana Instruments cryostation. Tunable single-frequency Ti:Sapphire (TIS-SF-777) and diode (CTL 1500 - TOPTICA Photonics AG) lasers were used to measure the Zeeman splitting of several lines in the $^4I_{15/2} \to {}^4I_{9/2}$ and $^4I_{15/2} \to {}^4I_{13/2}$ optical transitions of Er^{3+}, respectively.
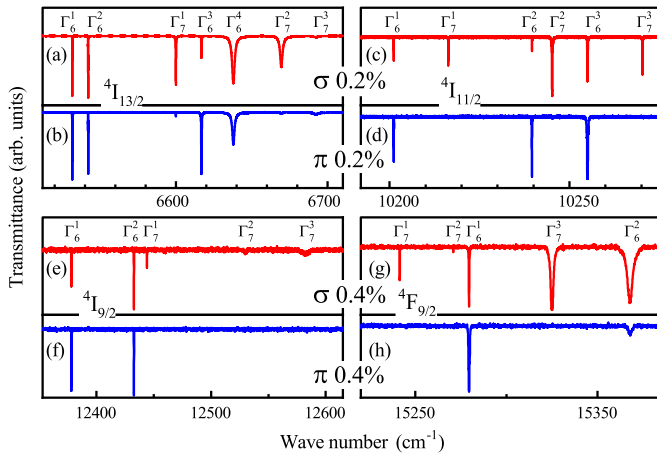
FIG. 2. High-resolution (0.01 cm^{-1}) (a),(c),(e),(g) σ- and (b),(d),(f),(h) π-polarized transmission spectra of YPO$_4$ single crystal doped with Er^{3+} in the regions of optical transitions from the ground state to the (a),(b) $^4I_{13/2}$, (c),(d) $^4I_{11/2}$, (e),(f) $^4I_{9/2}$, and (g),(h) $^4F_{9/2}$ CF multiplets at 5.3 K. Doping concentrations were (a),(b),(c),(d) 0.2 at.% and (e),(f),(g),(h) 0.4 at.%.

III. EXPERIMENTAL RESULTS

A. Crystal-field levels of Er^{3+} in Er : YPO$_4$

High-resolution transmission spectra and luminescence spectra in the earlier not explored infrared (IR) spectral region allowed us to complement the scheme of CF levels. Figures 2 and 3 present several examples of polarized IR transmission and luminescence spectra, respectively. We measured spectra of luminescence from the two lowest-energy CF states in each of the $^4I_{11/2}$ and $^4I_{13/2}$ multiplets to the CF levels of the ground $^4I_{15/2}$ multiplet, at excitation wavelength tuned to the $^4I_{15/2}(\Gamma_7^1) \rightarrow {}^4F_{9/2}(\Gamma_6^1)$ (15 279.4 cm^{-1}) transition. Intensity of the luminescence from $^4I_{11/2}$ was about two orders of magnitude lower than from $^4I_{13/2}$.

The impurity Er^{3+} ions in yttrium orthophosphate substitute for Y^{3+} ions at the sites with the tetragonal point symmetry group D_{2d}. The crystal field of the D_{2d} symmetry splits the energy levels of the free Er^{3+} ion characterized by the electronic total angular momentum J into $J + 1/2$ Kramers doublets, the wave functions of which transform according to Γ_6 and Γ_7 irreducible representations of the D_{2d} point group. Particular numbers of Γ_6 and Γ_7 levels for each J are indicated in Table I. The Kramers doublets can be further split by a magnetic field and we discuss this point later in Sec. III B.

The assignment of the observed spectral lines was based on the selection rules for electric dipole (ED) and magnetic dipole (MD) transitions at the sites with D_{2d} symmetry. These selection rules are given in Table II.

First of all, we check the symmetry of the ground state. At 5 K only this state is populated. Whatever the symmetry of the ground state is, in the σ polarization all transitions are ED allowed (see Table II). For the π-polarized spectrum, the situation is different, namely, $\Gamma_6 \rightarrow \Gamma_6$ and $\Gamma_7 \rightarrow \Gamma_7$ transitions are allowed only in the MD approximation. The MD contribution is, as a rule, weak, with the exception of the MD allowed in the free Er^{3+} ion $^4I_{13/2} \leftrightarrow {}^4I_{15/2}$ transition. If the symmetry of the ground state were Γ_6 (Γ_7), one would expect to observe three (two) absorption lines in the π-polarized spectra of multiplets with $J = 9/2$. Two lines in the π spectra of $^4I_{9/2}$ and $^4F_{9/2}$ multiplets in Fig. 2 are in favor of the Γ_7 symmetry of the ground state. Energies and symmetries of the CF levels in the excited multiplets found directly from the low-temperature polarized absorption spectra are listed in Table I.

The CF levels of the ground multiplet $^4I_{15/2}$ were found from the transmission spectra at elevated temperatures and from the luminescence spectra. These data are given in Table III, together with the corresponding literature data. As the ionic radii of Er^{3+} and Y^{3+} for coordination number VIII are close (0.1004 and 0.1019 nm, respectively [30]), CF levels of Er^{3+} in Er : YPO$_4$ and ErPO$_4$ vary little. For the ground
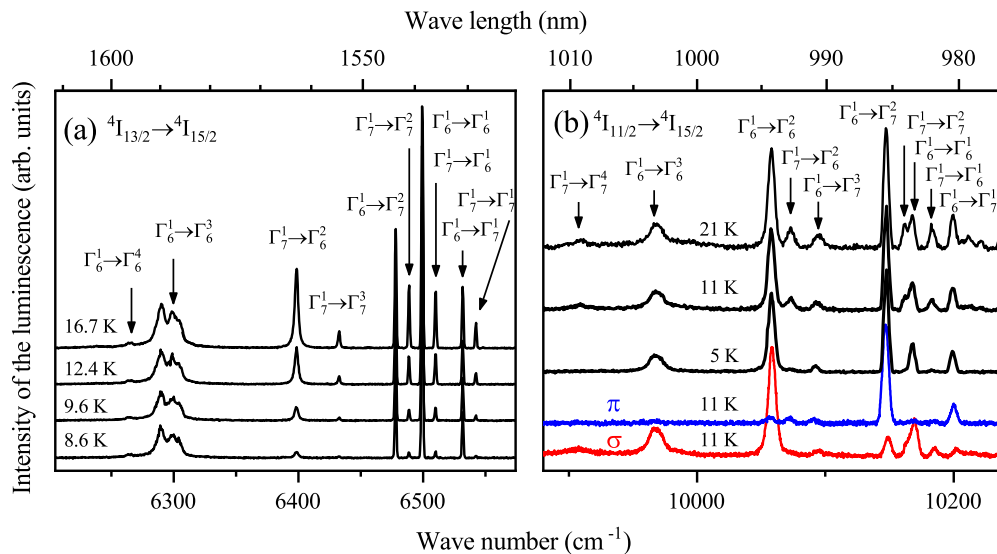

FIG. 3. Luminescence spectra of the YPO$_4$: Er^{3+} (0.2 at. %) single crystal in the regions of (a) $^4I_{13/2} \rightarrow {}^4I_{15/2}$ and (b) $^4I_{11/2} \rightarrow {}^4I_{15/2}$ optical transitions at different temperatures indicated above the spectra. Unpolarized (black lines), σ- (red line), and π- (blue line) polarized luminescence.

TABLE I. Energies (cm^{-1}) at 5 K and irreducible representations Γ of CF levels of Er^{3+} ions in Er : YPO$_4$ crystals for excited multiplets. Data from the absorption (Abs.) and luminescence (Lum.) experiments are compared with the results of calculations (Calc.).

	This work				This work		Ref. [24]		This work	Ref. [24]
Γ	Abs.	Lum.	Calc.	Γ	Abs.	Calc.	Abs.	Γ	Calc.	Abs.
$^4I_{13/2} \rightarrow 4\Gamma_6 + 3\Gamma_7$				$^4F_{9/2} \rightarrow 2\Gamma_6 + 3\Gamma_7$				$^4F_{5/2} \rightarrow 2\Gamma_6 + \Gamma_7$		
Γ_6^1	6531.6	6531.6	6537	Γ_7^1	15241.5	15245	15241.5	Γ_6^1	22161	22162.1
Γ_7^1	6542.0	6542	6545	Γ_7^2	15270.8	15280	15270.9	Γ_7^1	22193	22191.6
Γ_7^2	6599.9		6600	Γ_6^1	15279.5	15281	15279.4	Γ_6^2	22191	22195.5
Γ_6^2	6616.8		6617	Γ_7^3	15325.1	15324	15325	$^4F_{3/2} \rightarrow \Gamma_6 + \Gamma_7$		
Γ_6^3	6637.8		6641	Γ_6^2	15367.8	15367	15367.8	Γ_6^1	22520	22517
Γ_7^3	6669.5		6676	$^4S_{3/2} \rightarrow \Gamma_6 + \Gamma_7$				Γ_7^2	22548	22550.7
Γ_6^4	6692.3		6694	Γ_6^1	18367.3	18373	18367.1	$^2H_{9/2} \rightarrow 2\Gamma_6 + 3\Gamma_7$		
$^4I_{11/2} \rightarrow 3\Gamma_6 + 3\Gamma_7$				Γ_7^1	18416.7	18409	18416.3	Γ_6^1	24485	24502.7
Γ_6^1	10201.1	10201	10194	$^2H_{11/2} \rightarrow 3\Gamma_6 + 3\Gamma_7$				Γ_6^2	24548	24539
Γ_7^1	10216.3	10216	10209	Γ_6^1	19087.3	19095	19087.1	Γ_7^1	24539	24541.4
Γ_6^2	10239.6		10240	Γ_7^1		19130	19119.7	Γ_7^2	24608	24623.3
Γ_7^2	10245.2		10245	Γ_6^2	19145.8	19157	19145.8	Γ_7^3	24671	24656.2
Γ_6^3	10255.		10258	Γ_7^2	19183.3	19185	19183.4	$^4G_{11/2} \rightarrow 3\Gamma_6 + 3\Gamma_7$		
Γ_7^3	10270.4		10272	Γ_6^2	19202.2	19184	19201.8	Γ_6^1	26313	26310.3
$^4I_{9/2} \rightarrow 2\Gamma_6 + 3\Gamma_7$				7		19218	19235.3	Γ_7^1	26337	26332.5
Γ_6^1	12378.2		12371	$^4F_{7/2} \rightarrow 2\Gamma_6 + 2\Gamma_7$				Γ_6^2	26370	26353.3
Γ_6^2	12432.7		12442	Γ_7^1		20489	20484.7	Γ_7^2	26411	26405.4
Γ_7^1	12444.1		12446	Γ_6^1	20496.3	20492	20496.3	Γ_6^2	26455	26466.6
Γ_7^2	12530.6		12527	Γ_6^2	20557.8	20556	20557.6	Γ_7^3	26476	26485.5
Γ_7^3	12582.6		12595	Γ_7^2	20573.7	20569	20573.5			

multiplet, the latter were studied also by inelastic neutron [31] and resonance Raman [32] scatterings. Table III lists also these data.

Most of the measured energies of the CF sublevels of the ground and excited multiplets of the Er^{3+} ion and the corresponding irreducible representations determined from the polarized spectra (see Tables I and III) coincide with the earlier published data [24]. The energy value 138.3 cm^{-1} announced from neutron scattering experiments on ErPO$_4$ [31] disagrees with other data.

Measurements of the luminescence kinetics from the $^4I_{13/2}$ level revealed a single decay time $\tau = 5.1 \pm 0.2$ ms at 5 K (see details in the Appendix). For a comparison, erbium luminescence decay time 2.3 ms was observed in YVO$_4$:Er (2.5 at.%) [34].

B. EPR and magneto-optical spectroscopy: *g* factors

We confirm the values of the ground-state *g* factors from the angular dependences of the EPR spectra measured in the X

TABLE II. Selection rules for the ED and MD optical transitions of Kramers ions in the D_{2d} symmetry sites.

D_{2d}	Γ_6	Γ_7
Γ_6	$\sigma_{\text{ED,MD}}\ \pi_{\text{MD}}$	$\sigma_{\text{ED}}\ \pi_{\text{ED,MD}}$
Γ_7	$\sigma_{\text{ED}}\ \pi_{\text{ED,MD}}$	$\sigma_{\text{ED,MD}}\ \pi_{\text{MD}}$

band ($g_{0\parallel} = 6.42$ and $g_{0\perp} = 4.80$) is in good agreement with the values from the literature [35,36].

We now determine the *g* factors of several excited states from the analysis of the high-resolution absorption spectra of the Er : YPO$_4$ crystal placed into the magnetic fields $\mathbf{B}||c$ and $\mathbf{B}\perp c$. Figure 4(a) shows, as an example, the Zeeman splitting of the absorption line 6531.6 cm^{-1} in a magnetic field $\mathbf{B}||c$. The Zeeman splitting of the corresponding Kramers doublets and allowed transitions between them are displayed in the scheme of Fig. 4(b). Two (four) transitions are allowed in the σ (π) polarization. Of the four π-polarized transitions, two are ED transitions and the other two are MD ones (we should note that for the $^4I_{15/2} \rightarrow {}^4I_{13/2}$ transition, which is MD allowed in the free Er^{3+} ion, the intensity of the MD transitions between CF levels can be comparable with that of the ED transitions). It follows from the observed Zeeman spectral pattern [see Fig. 4(a)], in which the σ-polarized line splitting $\Delta\nu_\sigma$ coincides with the smallest of the two splittings of the π-polarized line, that the *g* factors of the ground and excited states have different signs (if the signs were the same, the σ-polarized lines would show a coincidence with the largest splitting of the π-polarized line). In this case, $\Delta\nu_\sigma = \Delta_0 - \Delta_{\text{ex}} = \Delta\nu_\pi^{\text{MD}}$; $\Delta\nu_\pi^{\text{ED}} = \Delta_0 + \Delta_{\text{ex}}$, where $\Delta_0 = |g_0|\mu_B B$ and $\Delta_{\text{ex}} = |g_{\text{ex}}|\mu_B B$ are the Zeeman splittings of the ground and excited Kramers doublets, respectively, and μ_B is the Bohr magneton. The inset of Fig. 4(a) shows the field dependences of the Zeeman splitting in the σ and π polarizations. From a linear fitting of these

TABLE III. Energies E (cm^{-1}) and symmetries Γ of CF levels of the Er^{3+} ions in Er : YPO$_4$, Er : LuPO$_4$, and ErPO$_4$ crystals for the ground multiplet $^4I_{15/2}$.

Er : YPO$_4$, this work						Er : YPO$_4$ [24]		Er: LuPO$_4$ [33]	ErPO$_4$ [32]	ErPO$_4$ [31]		ErPO$_4$ [32]	
Lum.		Abs.		Calc.		Abs.		Abs.	Abs.	Neutrons		Raman	
Γ	E	Γ	E	Γ	E	Γ	E	E	E	Γ	E	Γ	E
Γ_7^1	0	Γ_7^1	0	Γ_7^1	0	Γ_7^1	0	0	0	Γ_7^1	0	Γ_7^1	0
Γ_6^1	31	Γ_6^1	32	Γ_6^1	37	Γ_6^1	32	36	33	Γ_6^1	32.9	Γ_6^1	33
Γ_7^2	52	Γ_7^2	50	Γ_7^2	51	Γ_7^2	52.5	53	53	Γ_7^2	52.2	Γ_7^2	53
Γ_7^3	106	Γ_7^3	108	Γ_7^3	111	Γ_7^3	108	98	105	Γ_7^3	138.3	Γ_7^3	105
Γ_6^2	141	Γ_6^2	144	Γ_6^2	141	Γ_6^2	143		145	Γ_6^2	144.3	Γ_6^2	145
Γ_6^3	231	Γ_6^3		Γ_6^3	235	Γ_6^3			232	Γ_6^3	233.9	Γ_6^3	234
Γ_7^4	264	Γ_7^4		Γ_7^4	250	Γ_7^4			244	Γ_7^4	242.3	Γ_7^4	246
Γ_6^4	303	Γ_6^4		Γ_6^4	306	Γ_6^4				Γ_6^4		Γ_6^4	269

dependences, we find values and signs of g_{ex}, under an assumption that g_0 is positive. A summary of the results is given in Table IV.
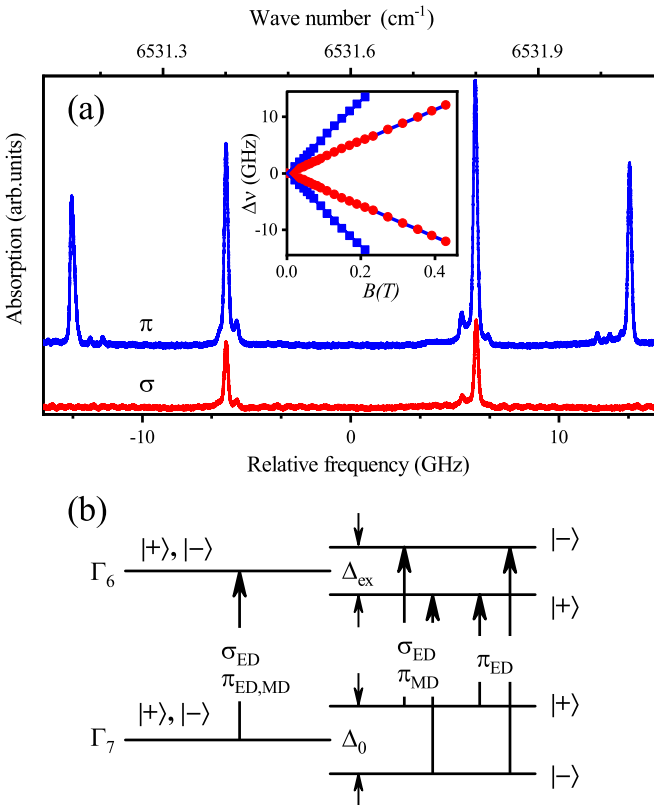

FIG. 4. (a) Zeeman splitting of the spectral line 6531.6 cm^{-1} corresponding to the $\Gamma_7^1(^4I_{15/2}) \rightarrow \Gamma_6^1(^4I_{13/2})$ optical transition of Er^{3+} in YPO$_4$: Er (0.01 at.%) subjected to a magnetic field **B**||c, $B = 0.21$ T in the σ (red lower trace) and π (blue upper trace) polarizations. Inset: Field dependences of the Zeeman splittings $\Delta\nu_\sigma$ (red symbols) and $\Delta\nu_\pi$ (blue symbols and line) in the σ and π polarizations, respectively. $T = 5$ K. (b) Scheme showing Zeeman splitting of the corresponding Kramers doublets and allowed transitions between them.

C. Hyperfine structure in the EPR and optical spectra of Er : YPO$_4$

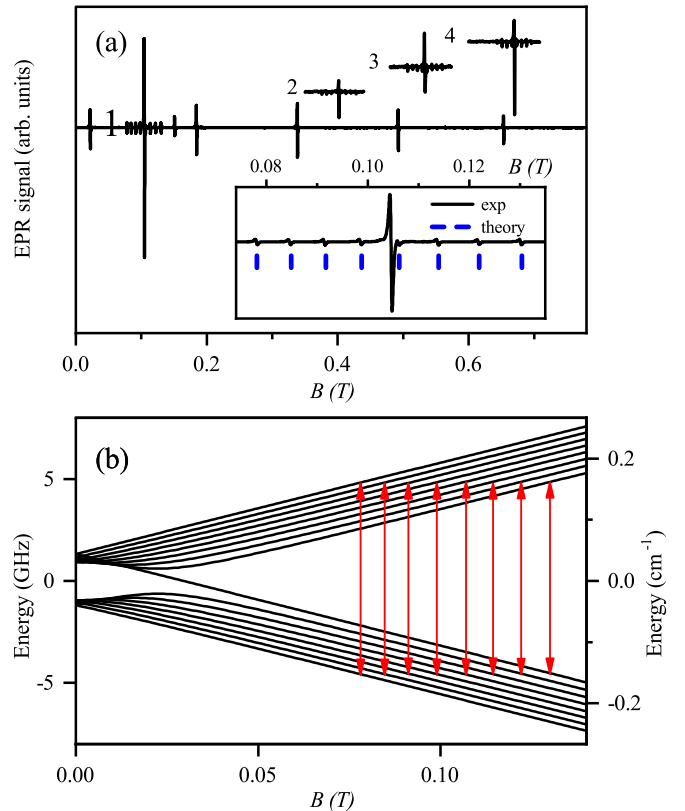Figure 5(a) displays high-resolution EPR spectra of a YPO$_4$:Er (0.1%) sample obtained with both a Bruker

FIG. 5. (a) EPR spectra of the YPO$_4$:Er (0.1%) single crystal in the **B**||c orientation of an external magnetic field, at the frequencies (1) 9.4 GHz; (2) 36.3 GHz, (3) 48 GHz, (4) 60.2 GHz. $T = 5$ K (1), $T = 4.2$ K (2–4). Inset: spectrum 1 in more detail; blue vertical lines represent positions of the calculated hyperfine components. (b) Calculated hyperfine energy levels corresponding to the ground $^4I_{15/2}(\Gamma_7^1)$ Kramers doublet in a magnetic field. The arrows indicate EPR transitions at the frequency 9.4 GHz. The calculations are detailed in Sec. IV.

TABLE IV. Experimental and calculated values of the g factors for Er^{3+} in Er : YPO_4. Signs of g were determined relative to the ground Kramers doublet.

Multiplet	E, cm^{-1}	Γ	$g_{\parallel}$ Exp.	Calc.	$g_{\perp}$ Exp.	Calc.	Type of the transition the ground state Γ_7^1 ($^4I_{15/2}$) π-pol.	σ-pol.
			6.42 ± 0.02		4.80 ± 0.02			
$^4I_{15/2}$	0	Γ_7^1	6.438 [35]	6.78	4.803 [35]	4.71	–	–
			6.42 [36]		4.81 [36]			
$^4I_{13/2}$	6531.6	Γ_6^1	-2.6 ± 0.1	-2.65	6.8 ± 0.1	6.93	ED,MD	ED
	6542	Γ_7^1	4.5 ± 0.1	4.48	-4.4 ± 0.1	-4.59	MD	ED,MD
	6600	Γ_7^2	-5.2 ± 0.1	-5.56	3.7 ± 0.1	3.96	MD	ED,MD
	6617	Γ_6^2	-6.0 ± 0.1	-5.87	-4.3 ± 0.1	-4.12	ED,MD	ED
$^4I_{9/2}$	12378	Γ_6^1	-3.2 ± 0.1	-2.72	3.0 ± 0.1	3.50	ED,MD	ED
	12432.7	Γ_6^2	1.3 ± 0.1	1.00	-3.0 ± 0.1	-3.50	ED,MD	ED

EMX-plus X-band and a homemade broadband spectrometers in the $B||c$ geometry. Well-resolved hyperfine structure (HFS) of the ^{167}Er isotope with nuclear spin $I = 7/2$ is observed. The inset of Fig. 5(a) demonstrates in more detail the HFS in the EPR spectrum at the frequency 9.4 GHz and the scheme of Fig. 5(b) illustrates the origin of this HFS. Measurements at higher frequencies show that the widths of the erbium lines do not change.

In optical spectra, only partly resolved HFS is observed, due to relatively large inhomogeneous line broadening. In Fig. 6(a), where the 6531.6 cm^{-1} absorption line of Er^{3+} in YPO_4:Er (0.005 at.%) registered at a low temperature and a zero external field by a tunable single-frequency laser with the spectral resolution $\sim 5 \times 10^{-5}$ cm^{-1} is presented, the finest spectral details have the width ~ 0.005 cm^{-1}. These details smear out with growing erbium concentration in Er : YPO_4, due to an increasing inhomogeneous line broadening. In

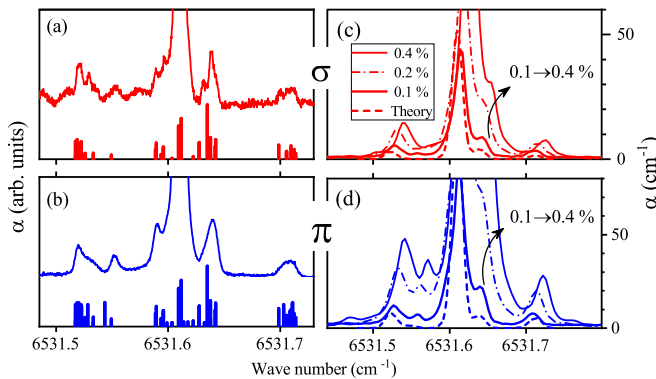FIG. 6. The 6531.6 cm^{-1} absorption line of Er^{3+} in Er : YPO_4 registered at $T = 5$ K, $B = 0$ (a),(b) by a tunable single-frequency laser, Er concentration 0.005 at.% and (c),(d) by a high-resolution Fourier spectrometer, thick solid, dash-dotted, and thin solid spectral traces represent the data for 0.1, 0.2, and 0.4 at.% of erbium, respectively. (a),(c) σ and (b),(d) π polarizations. Bars in (a) and (b) represent the calculated hyperfine structure in the spectra of ^{167}Er^{3+}; the dashed lines in (c) and (d) show the results of modeling (the linewidth of 7×10–3 cm^{-1} was attributed to each hyperfine component of the line, to account for the inhomogeneous broadening, see the text).

particular, the spectra of Er : YPO_4 with erbium concentrations 0.1, 0.2, and 0.4 at.% [see Fig. 6(c)] did not change when the spectrometer's resolution was lowered from 0.005 to 0.02 cm^{-1}. The observed HFS provides a tool for checking the quality of the crystal-field parameters obtained in the crystal-field calculations based on our high-resolution spectroscopy data and described in the next section.

IV. CALCULATIONS OF ENERGY LEVELS, SPECTRA, AND HYPERFINE STRUCTURE

The Hamiltonian of the Er^{3+} ion operating in the basis of 364 states of the ground $4f^{11}$ electronic configuration contains the free-ion standard Hamiltonian H_{FI} and the crystal-field Hamiltonian H_{CF}:

$$H = H_{\mathrm{FI}} + H_{\mathrm{CF}}. \qquad (1)$$

H_{FI} is constructed from the effective operators following conventional notations of the spectroscopic theory of lanthanides [37]:

$$H_{\mathrm{FI}} = H_0 + \sum_{k=0,2,4,6} F^k f_k + \zeta A_{SO} + \alpha L(L+1)$$
$$+ \beta G(G_2) + \gamma G(R_7) + \sum_{i=2,3,4,6,7,8} T^i t_i$$
$$+ \sum_{j=0,2,4} M^j m_j + \sum_{s=2,4,6} P^s p_s. \qquad (2)$$

Here, H_0 is spherically symmetric one-electron part of the Hamiltonian, F^k and ζ are electrostatic and spin-orbit integrals, f_k and A_{SO} represent the angular parts of the electrostatic and spin-orbit interaction, respectively. The parameters associated with the two-body electrostatic correlation terms are denoted by α, β, and γ; L is the total orbital angular momentum, $G(G_2)$ and $G(R_7)$ are Casimir's operators [38]. Three-body electrostatic interaction terms are parametrized by T^i ($i = 2, 3, 4, 6, 7, 8$) [39]. The last two terms in Eq. (2) represent magnetically correlated corrections [40]: they include spin-spin and spin-other-orbit relativistic corrections parametrized by M^j ($j = 0, 2, 4$), and electrostatically correlated spin-orbit perturbation parametrized by P^s ($s = 2, 4, 6$).

TABLE V. Parameters of the free-ion Hamiltonian used in the present work (standard notations, see Ref. [37]), cm^{-1}.

F^2	F^4	F^6	ζ	α	β	γ	T^2	T^3	T^4
96589	67938	54360	2366.3	17.60	-577	1813	465	52.5	92
T^6	T^7	T^8	M^0	M^2	M^4	P^2	P^4	P^6	
-234	275	308	4.01	2.86	1.95	657	434	0	

The crystal-field interaction is expressed via Stevens operators O_p^k [41]:

$$H_{CF} = \sum_{pk} B_p^k O_p^k. \tag{3}$$

In the case of the D_{2d} local symmetry, only the parameters B_2^0, B_4^0, B_4^4, B_6^0, and B_6^4 have nonzero values.

Matrices of the effective operators contained in Eqs. (2) and (3) in the basis of 364 states of $4f^{11}$ electronic configuration have been numerically calculated in our previous studies [42,43]. The 364 electronic eigenstates have been found by numerical diagonalization of the matrix of the Hamiltonian (1). The parameters of the free-ion Hamiltonian have been initially set to equal those of Er : LiYF$_4$ crystal [43], while the CF parameters B_p^k have been chosen according to Ref. [24]. After that, all 24 parameters of the model Hamiltonian have been varied to achieve the best agreement with the whole set of the experimental data, i.e., the transition energies and g factors of the Kramers states in Er : YPO$_4$ crystal. The final set of parameters thus obtained is presented in Tables V and VI. The calculated CF energies are given in Tables I and III and the calculated g factors are in Table IV, to be compared with the experimental data.

In order to reproduce the hyperfine structure observed for the $^4I_{15/2} \rightarrow {}^4I_{13/2}$ transition (see Fig. 6), the magnetic part of the hyperfine interaction of ^{167}Er isotope (22.9%) with nuclear spin $I = 7/2$ was taken into account [44]:

$$H_{HFM} = \mu_B \gamma_N \hbar \left\langle \frac{1}{r^3} \right\rangle_{4f} \sum \{ 2Il + O_2^0(3s_zI_z - sI)$$
$$+ 3O_2^2(s_xI_x - s_yI_y) + 3O_2^{-2}(s_xI_y + s_yI_x)$$
$$+ 6O_2^1(s_xI_z + s_zI_x) + 6O_2^{-1}(s_zI_y + s_yI_z) \}. \tag{4}$$

The sums above are taken over $4f$ electrons, l and s are the one-electron orbital and spin moments, respectively, and $\gamma_N/2\pi = -1.23$ MHz/T is the gyromagnetic ratio of the ^{167}Er nucleus. The expectation value of $1/r^3$ operator of the $4f$ electrons, $\langle 1/r^3 \rangle_{4f}$, equals 11.07 at. units [44].
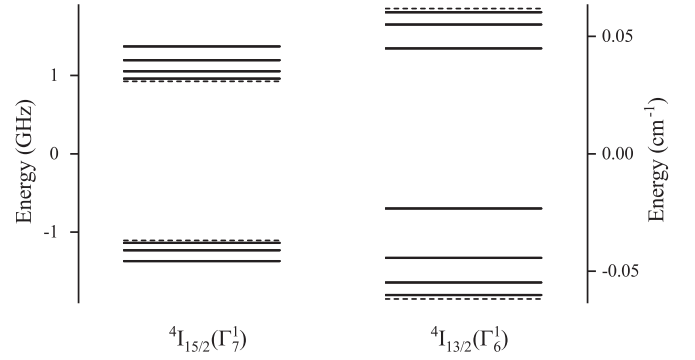

FIG. 7. The calculated ($B = 0$) hyperfine structure schemes of the ground Kramers doublet (left) and of the lowest-energy Kramers doublet in the $^4I_{13/2}$ multiplet (right) of ^{167}Er in YPO$_4$, involved in the formation of HFS of the spectral line 6531.6 cm^{-1}. Doublet (singlet) hyperfine levels are represented by solid (dotted) lines.

The lower part of the basis of 364 electronic eigenstates found by numerical diagonalization of the Hamiltonian (1) corresponding to the energy band 0–16 000 cm^{-1} was used to form a truncated space of 62 states (the lowest 5 multiplets). The total Hamiltonian $H_{tot} = H_{FI} + H_{CF} + H_{HFM}$ was projected onto the basis of $62 \times 8 = 496$ electron-nuclear states and then diagonalized numerically. In such a way, energies and wave functions of hyperfine sublevels were found. The calculated hyperfine structure of the Kramers doublets involved in the 6531.6 cm^{-1} transition is shown in Fig. 7. Each Kramers doublet breaks into seven doublets and two singlets (16 hyperfine states in total). A superposition of wave functions with different values of m (where m is the nuclear spin projection, $-7/2 \leqslant m \leqslant 7/2$) corresponds to each hyperfine level (which is a peculiarity of Kramers ions, see, e.g., Ref. [45]). Because of that, plenty of transitions obeying the $\Delta m = 0$ selection rule take place. Table VII lists all the allowed transitions.

The transition probabilities were determined by the electric dipole and magnetic dipole line strengths, which, for a given hyperfine transition $|i\rangle \rightarrow |f\rangle$, equal

$$S_{if,q}^{(ED)} = |\langle i|d_q|f \rangle|^2, \quad S_{if,q'}^{(MD)} = |\langle i|\mu_{q'}|f \rangle|^2, \tag{5}$$

where q and q' denote the polarization of the electric and magnetic field, respectively, $\boldsymbol{\mu} = -\mu_B(\mathbf{L} + 2\mathbf{S})$ is the magnetic moment and $\mathbf{d}$ is the effective electric moment of the Er^{3+} ion, which contains odd CF operators that admix wave functions of different parity to the $4f$ wave functions. The calculation of the magnetic dipole line strengths is straightforward. In our calculations of the electric dipole line strengths, we took into account the $4f \leftrightarrow 5d$ configuration mixing and followed

TABLE VI. The crystal-field parameters B_p^k(cm^{-1}) for Er^{3+} in Er : YPO$_4$.

p	K	B_p^k		
		Present work	Ref. [24]	Ref. [25]
2	0	112.9	141	185
4	0	10.3	18.1	18
4	4	776	837	800
6	0	-43.0	-40.4	-40.4
6	4	56.1	89	88

TABLE VII. Energy levels and allowed $i \rightarrow f$ transitions between the hyperfine sublevels of the ground $^4I_{15/2}(\Gamma_7^1)$ and excited $^4I_{13/2}(\Gamma_6^1)$ Kramers states in π and σ polarizations. Values of i are determined by the first column, while the allowed f values are presented in the last three columns. Energies of the hyperfine sublevels shown in Fig. 7 are given with respect to the mean energy of the Kramers doublet. The energies of the doublet states are in bold.

HF level No.	Energy of i-th state of $^4I_{15/2}(\Gamma_7^1)$, GHz	Energy of f-th state of $^4I_{13/2}(\Gamma_6^1)$, GHz	Allowed transitions to the excited state f		
			π_{ED}	π_{MD}	σ_{ED}
1	**−1.37**	−1.86	4, 6	3, 5, 7	3, 5, 7
2	**−1.23**	**−1.81**	3, 7	2, 4, 6, 8	2, 4, 6, 8
3	**−1.14**	**−1.64**	2, 8	1, 3, 7, 9	1, 3, 7, 9
4	−1.11	**−1.33**	9	2, 8	2, 8
5	0.93	**−0.70**	1	2, 8	2, 8
6	**0.96**	**1.35**	2, 8	1, 3, 7, 9	1, 3, 7, 9
7	**1.06**	**1.65**	3, 7	2, 4, 6, 8	2, 4, 6, 8
8	**1.20**	**1.81**	4, 6	3, 5, 7	3, 5, 7
9	**1.37**	1.86	5	4, 6	4, 6

the line of Ref. [43]. In Figs. 6(a) and 6(b), the results of calculations are represented by the bars located at calculated frequencies and of the highs proportional to the calculated line strengths. In Figs. 6(c) and 6(d), the linewidth (full width at half height) of 7×10^{-3} cm^{-1} (200 MHz) was attributed to each hyperfine component of the line, to account for the inhomogeneous broadening. There is a good agreement between the experimental and calculated hyperfine patterns in the optical spectra, which testifies a good quality of the crystal-field parameters obtained in our study.

In order to account for the hyperfine structure in the EPR spectra corresponding to microwave transitions within the lowest Kramers doublet $^4I_{15/2}(\Gamma_7^1)$ (Fig. 5), the hyperfine interaction operator (4) and Zeeman interaction with the external magnetic field $\mathbf{B}_0$, $H_Z = -\boldsymbol{\mu}\mathbf{B}_0$, were projected onto the lowest two eigenstates of the Hamiltonian (1):

$$H' = H_Z + H_{HFM} = g_\parallel \mu_B B_{0z} S'_z + g_\perp \mu_B (B_{0x} S'_x + B_{0y} S'_y)$$
$$+ A_\parallel S'_z I_z + A_\perp (S'_x I_x + S'_y I_y), \quad (6)$$

where $S' = 1/2$ is the effective spin, $g_\parallel = 6.78$ and $g_\perp = 4.71$ are the calculated g factors, $A_\parallel = 730$ MHz and $A_\perp = 509$ MHz are the hyperfine parameters, all corresponding to the lowest Kramers doublet. These calculated values are in reasonable agreement with the EPR data published previously [35].

Calculated positions of the hyperfine components in the EPR spectra of Er : YPO$_4$ (shown in the inset of Fig. 5) practically coincide with the experimental ones. Based on good results of modeling the hyperfine patterns in the high-resolution optical and EPR spectra of Er^{3+} in YPO$_4$, we suggest that a reliable set of energies of hyperfine levels (necessary for applications in quantum technologies) can be calculated using the crystal field and other parameters obtained in this study.

V. SUMMARY

We have performed high-resolution (up to $\sim 5 \times 10^{-5}$ cm^{-1}) broadband (5 000–21 000 cm^{-1}) temperature-dependent (5–300 K) polarized transmission and infrared (0.9–1.6 μm) luminescence measurements of yttrium orthophosphate single crystals doped with erbium. The Er : YPO$_4$ samples with Er concentrations 0.005, 0.01, 0.1, 0.2, 0.4, and 0.7 at.% were studied. Zeeman splittings in the $^4I_{15/2} \rightarrow {}^4I_{9/2}$ and $^4I_{15/2} \rightarrow {}^4I_{13/2}$ absorption manifolds in magnetic fields $\mathbf{B}||c$ and $\mathbf{B}\perp c$, as well as X-band and high-frequency (36–76 GHz) EPR spectra were also investigated.

Energies and symmetries of 40 crystal-field Kramers doublets and g factors for the levels 6531.6, 6542, 6600, 6617, 12378, and 12432.7 cm^{-1} were determined. These data were taken as a base for the CF calculations. We have observed the electron-nuclear hyperfine structure in the EPR and optical spectra of Er : YPO$_4$ and were able to successfully model it using the wave functions obtained from the CF calculations. The results of the present study pave the way for potential applications in quantum electronics and quantum information processing at telecom wavelength.
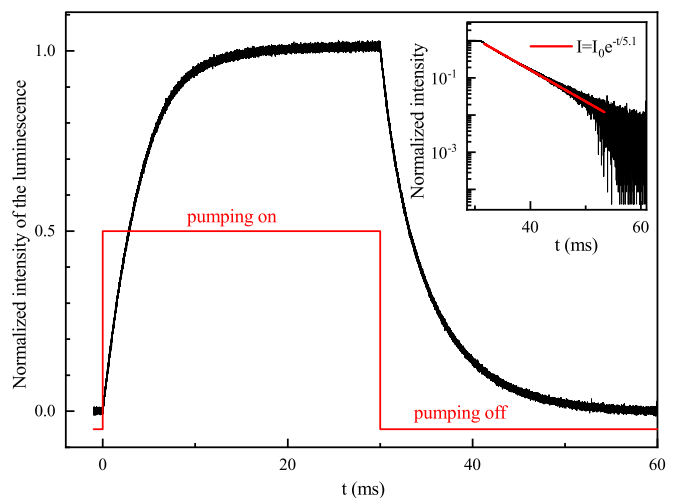

FIG. 8. $^4I_{13/2} \rightarrow {}^4I_{15/2}$ luminescence excitation and decay of Er^{3+} in YPO$_4$:Er (0.1 at.%) at $T = 5$ K. Inset: Luminescence decay in a logarithmic scale and exponential approximation (red line) with lifetime 5.1 ± 0.2 ms.

APPENDIX: LIFETIME OF THE $^4I_{13/2}$ STATE

We have measured the decay times of the $^4I_{13/2} \rightarrow {}^4I_{15/2}$ luminescence of Er^{3+} in YPO_4 at low temperature (5 K) for the sample YPO_4:Er (0.1 at.%). Figure 8 shows the decay curve. A single exponent with $\tau = 5.1 \pm 0.2$ ms is observed (see the inset of Fig. 8).

[1] H. Yu, J. Liu, H. Zhang, A. A. Kaminskii, Z. Wang, and J. Wang, Advances in vanadate laser crystals at a lasing wavelength of 1 micrometer, Laser Photon. Rev. **8**, 847 (2014).

[2] R. Lisiecki, P. Solarz, G. Dominiak-Dzik, W. Ryba-Romanowski, M. Sobczyk, P. Černý, J. Šulc, H. Jelínková, Y. Urata, and M. Higuchi, Comparative optical study of thulium-doped YVO_4, $GdVO_4$, and $LuVO_4$ single crystals, Phys. Rev. B **74**, 035103 (2006).

[3] F. Di. Trapani, X. Mateos, V. Petrov, A. Agnesi, U. Griebner, H. Zhang, J. Wang, and H. Yu, Continuous-wave laser performance of Tm : $LuVO_4$ under Ti:sapphire laser pumping, Laser Phys. **24**, 035806 (2014).

[4] J. Liu, X. Chen, W. Han, D. Zhong, S. Zhang, and B. Teng, Columnar crystal of Yb : $LuPO_4$ for high-power miniature rod lasers, Opt. Mater. Express **5**, 2437 (2015).

[5] L. Wang, X. Dou, W. Han, H. Xu, D. Zhong, B. Teng, and J. Liu, Repetitively Q-switched laser operation of miniature Yb:LuPO4 crystal rod, Opt. Mater. Express **7**, 1048 (2017).

[6] L. Yang, B. Teng, D. Zhong, W. Han, J. He, Y. Xu, M. Zhu, J. Tang, S. Ji, and J. Liu, Growth, spectroscopic properties, and laser action of Yb : YPO_4 crystal, Opt. Mater. Express **7**, 3618 (2017).

[7] A. A. Kaminskii, M. Bettinelli, A. Speghini, H. Rhee, H. J. Eichler, and G. Mariotto, Tetragonal YPO_4 – a novel SRS-active crystal, Laser Phys. Lett. **5**, 367 (2008).

[8] V. N. Makhov, N. Yu. Kirikova, M. Kirm, J. C. Krupa, P. Liblik, A. Lushchik, Ch. Lushchik, E. Negodin, and G. Zimmerer, Luminescence properties of YPO_4:Nd^{3+}: A promising VUV scintillator material, Nucl. Instrum. Methods A **486**, 437 (2002).

[9] P. S. Peijzel, P. Vergeer, A. Meijerink, M. F. Reid, L. A. Boatner, and G. W. Burdick, $4f^{n-1}5d \rightarrow 4f^n$ emission of Ce^{3+}, Pr^{3+}, Nd^{3+}, Er^{3+}, and Tm^{3+} in $LiYF_4$ and YPO_4, Phys. Rev. B **71**, 045116 (2005).

[10] X. Zhang, Z. Fu, Z. Sun, G. Liu, J. H. Jeong, and Z. Wu, Temperature-induced phase transition and temperature sensing behavior in Yb^{3+} sensitized Er^{3+} doped YPO_4 phosphors, Opt. Mater. **60**, 526 (2016).

[11] P. Vergeer, T. J. H. Vlugt, M. H. F. Kox, M. I. den Hertog, J. P. J. M. van der Eerden, and A. Meijerink, Quantum cutting by cooperative energy transfer in $Yb_xY_{1-x}PO_4$: Tb^{3+}, Phys. Rev. B **71**, 014119 (2005).

[12] L. Xie, Y. Wang, and H. Zhang, Near-infrared quantum cutting in YPO_4:Yb^{3+}, Tm^{3+} via cooperative energy transfer, Appl. Phys. Lett. **94**, 061905 (2009).

[13] T. Grzyb, A. Gruszeczka, and S. Lis, Up-conversion luminescence of Yb^{3+} and Er^{3+} doped YPO_4, $LaPO_4$ and $GdPO_4$ nanocrystals, J. Lumin. **175**, 21 (2016).

[14] S. I. Rivera, F. J. Carrillo, A. García, and J. Oliva, Up-conversion of luminescence in YPO_4:Er^{3+} powders. A new technique, Mater. Lett. **187**, 83 (2017).

[15] P. A. Ryabochkina, S. A. Antoshkina, A. S. Vanetsev, I. Sildos, O. M. Gaitko, V. M. Kyashkin, S. N. Ushakov, A. A. Panov, N. Yu Tabachkova, and K. N. Nishchev, Synthesis, spectroscopic and luminescent properties of nanosized powders of yttrium phosphates doped with Er^{3+} ions, J. Nanopart. Res. **16**, 2326 (2014).

[16] N. Sangouard, C. Simon, H. de Riedmatten, and N. Gisin, Quantum repeaters based on atomic ensembles and linear optics, Rev. Mod. Phys. **83**, 33 (2011).

[17] F. Bussières, Ch. Clausen, A. Tiranov, B. Korzh, V. B. Verma, S. W. Nam, F. Marsili, A. Ferrier, Ph. Goldner, H. Herrmann, Ch. Silberhorn, W. Sohler, M. Afzelius, and N. Gisin, Quantum teleportation from a telecom-wavelength photon to a solid-state quantum memory, Nat. Photon. **8**, 775 (2014).

[18] P. Goldner, A. Ferrier, and O. Guillot-Noël, Rare earth-doped crystals for quantum information processing, *Handbook on the Physics and Chemistry of Rare Earths* (Elsevier, Amsterdam, 2015), Vol. 46, Chap. 267, pp. 1–78.

[19] H. de Riedmatten, M. Afzelius, M. U. Staudt, C. Simon, and N. Gisin, A solid-state light–matter interface at the single-photon level, Nature (London) **456**, 773 (2008).

[20] Z.-Q. Zhou, W.-B. Lin, M. Yang, C.-F. Li, and G.-C. Guo, Realization of Reliable Solid-State Quantum Memory for Photonic Polarization Qubit, Phys. Rev. Lett. **108**, 190505 (2012).

[21] M. Mazzera, R. Capelletti, A. Baraldi, E. Buffagni, N. Magnani, and M. Bettinelli, Hyperfine structure of Ho^{3+} levels and electron–phonon coupling in YPO_4 single crystals, J. Phys. Condens. Matter **24**, 205501 (2012).

[22] S.A. Moiseev, Off-resonant Raman-echo quantum memory for inhomogeneously broadened atoms in the cavity, Phys. Rev. A **88**, 012304 (2013).

[23] M. P. Hedges, J. J. Longdell, Y. L, and M. J. Sellars, Efficient quantum memory for light, Nature (London) **465**, 1052 (2010).

[24] D. Kuze, Optische absorptionsspektren und kristallfeldaufspaltungen des Er^{3+}-Ions in YPO_4 und YVO_4, Z. Phys. **203**, 49 (1967).

[25] Vishwamittar and S. P. Puri, Analysis of the behavior of Er^{3+} in zircon-structure systems, Phys. Rev. B **9**, 4673 (1974).

[26] H. Liu-Sen, W. Jun, Y. Min, and X. Shang-Da, Simulation of the f-d transitions of lanthanide ions in YPO_4 using quantum-chemical calculations, Chin. Phys. B **21**, 017801 (2012).

[27] R. Maâlej, M. Dammak, S. Kamoun, J.-L. Deschanvres, and M. Kamoun, Optical and crystal-field analysis of Er^{3+} ion in Y_2O_3–P_2O_5 thin films, J. Lumin. **126**, 165 (2007).

[28] R. S. Feigelson, Synthesis and single-crystal growth of rare-earth orthophosphates, J. Am. Ceram. Soc. **47**, 257 (1964).

[29] V. F. Tarasov and G. S. Shakurov, Submillimetre EPR spectrometer, Appl. Magn. Reson. **2**, 571 (1991).

[30] R. D. Schannon, Revised effective ionic radii and systematic studies of interatomic distances in halides and chalcogenides, Acta Cryst. **A32**, 751 (1976).

[31] C.-K. Loong, L. Soderholm, J. P. Hammonds, M. M. Abraham, L. A. Boatner, and N. M. Edelstein, Rare-earth energy levels and magnetic properties of HoPO$_4$ and ErPO$_4$, J. Phys. Condens. Matter **5**, 5121 (1993).

[32] P. C. Becker, G. M. Williams, R. E. Russo, N. Edelstein, J. A. Koningstein, L. A. Boatner, and M. M. Abraham, Resonance electronic Raman scattering in erbium phosphate crystals, Opt. Lett. **11**, 282 (1986).

[33] T. Hayhurst, G. Shalimoff, N. Edelstein, L. A. Boatner, and M. M. Abraham, Optical spectra and Zeeman effect for Er^{3+} in LuPO$_4$ and HfSiO$_4$, J. Chem. Phys. **74**, 5449 (1981).

[34] J. A. Capobianco, P. Kabro, F. S. Ermeneux, R. Moncorgé, M. Bettinelli, and E. Cavalli, Optical spectroscopy, fluorescence dynamics and crystal-field analysis of Er^{3+} in YVO$_4$, Chem. Phys. **214**, 329 (1997).

[35] M. M. Abraham, L. A. Boatner, J. O. Ramey, and M. Rappaz, An EPR study of rare-earth impurities in single crystals of the zircon-structure orthophosphates ScPO$_4$, YPO$_4$, and LuPO$_4$, J. Chem. Phys. **78**, 3 (1983).

[36] M. Dzionara, H. G. Kahle, and F. Schedewie, Paramagnetic resonance of Er^{3+} in YPO$_4$, Phys. Stat. Solidi B **47**, 135 (1971).

[37] W. T. Carnall, G. L. Goodman, K. Rajnak, and R. S. Rana, A systematic analysis of the spectra of the lanthanides doped into single crystal LaF$_3$, J. Chem. Phys. **90**, 3443 (1989).

[38] K. Rajnak and B. G. Wybourne, Configuration interaction effects in l^N configurations, Phys. Rev. **132**, 280 (1965).

[39] H. Crosswhite, H. M. Crosswhite, and B. R. Judd, Magnetic parameters for the configuration f^3, Phys. Rev. **174**, 89 (1968).

[40] B. R. Judd, H. M. Crosswhite, and H. Crosswhite, Intra-atomic magnetic interactions for f electrons, Phys. Rev. **169**, 130 (1968).

[41] B. Z. Malkin, Crystal field and electron-phonon interaction in the rare-earth ionic paramagnets, in *Spectroscopy of Crystals Containing Rare-Earth Ions*, edited by A. A. Kaplyanskii and R. M. Macfarlane (North-Holland, Amsterdam, 1987), p. 13.

[42] M. N. Popova, E. P. Chukalina, B. Z. Malkin, and S. K. Saikin, Experimental and theoretical study of the crystal-field levels and hyperfine and electron-phonon interactions in LiYF$_4$:Er^{3+}, Phys. Rev. B **61**, 7421 (2000).

[43] K. I. Gerasimov, M. M. Minnegaliev, B. Z. Malkin, E. I. Baibekov, and S. A. Moiseev, High-resolution magneto-optical spectroscopy of ^{7}LiYF$_4$:^{167}Er^{3+}, ^{166}Er^{3+} and analysis of hyperfine structure of ultranarrow optical transitions, Phys. Rev. B **94**, 054429 (2016).

[44] A. Abragam and B. Bleaney, *Electron Paramagnetic Resonance of Transition Ions* (Oxford University Press, Oxford, 1970).

[45] E. P. Chukalina and M. N. Popova, Hyperfine structure of infrared transitions in LiYF4 : Er^{3+}, Phys. Lett. A **262**, 191 (1999).